Engineering 23 (2023) 157–169

Contents lists available at ScienceDirect

Engineering

journal homepage: www.elsevier.com/locate/eng

Research
Advanced Antennas for Wireless Connectivity—Article

Diversity Glass Antennas for Tri-Band WiFi Applications

Peng Fei Hu [a,b,c,d], Kwok Wa Leung [a,b,c,d,*], Kwai Man Luk [a,d], Yong Mei Pan [e], Shao Yong Zheng [b,c]

[a] State Key Laboratory of Terahertz and Millimeter Waves and Department of Electrical Engineering, City University of Hong Kong, Hong Kong 999077, China
[b] School of Electronics and Information Technology (School of Microelectronics), Sun Yat-sen University, Guangzhou 510006, China
[c] Guangdong Provincial Key Laboratory of Optoelectronic Information Processing Chips and Systems, Sun Yat-sen University, Guangzhou 510006, China
[d] Information and Communication Technology Center, CityU Shenzhen Research Institute, Shenzhen 518057, China
[e] School of Electronic and Information Engineering, South China University of Technology, Guangzhou 510630, China

ARTICLE INFO

Article history:
Received 10 December 2021
Revised 25 April 2022
Accepted 1 September 2022
Available online 14 November 2022

Keywords:
Wireless fidelity
Diversity antennas
Multi-frequency
Glass
Dielectric resonator antennas
Multiple-input multiple-output

ABSTRACT

This paper investigates two novel polarization- and pattern-diversity glass dielectric resonator antennas (DRAs), both of which are for tri-band (2.4, 5.2, and 5.8 GHz) wireless fidelity (WiFi) applications. It also investigates what type of diversity antenna is most suitable for WiFi router applications by comparing the two DRAs, along with a new space-diversity glass DRA. These three diversity glass DRAs are also compared with a commercial space-diversity monopole pair to benchmark the performance of the glass DRA in WiFi router applications. In our polarization-diversity antenna, a double-port feeding scheme is developed to excite different DRA modes. The frequencies of the DRA modes are tuned by using a stepped DRA. For the pattern-diversity design, a stacked DRA is introduced to broaden the bandwidth for both the conical and broadside radiation modes. All three of the new diversity antennas were fabricated and measured to verify the simulations. In our experiment, the bit error rate (BER) of the three diversity glass antennas and the reference space-diversity monopole antenna was also measured, and the results are compared and discussed. It is found that the polarization-diversity omnidirectional DRA has the most stable BER among the three.

© 2022 THE AUTHORS. Published by Elsevier LTD on behalf of Chinese Academy of Engineering and Higher Education Press Limited Company. This is an open access article under the CC BY-NC-ND license (http://creativecommons.org/licenses/by-nc-nd/4.0/).

1. Introduction

Diversity antennas have multiple antenna ports operating at the same frequency. They can improve the channel capacity by transmitting independent data streams [1]. In general, there are three kinds of diversity antennas: polarization-, pattern-, and space-diversity antennas. Multiple-input multiple-output (MIMO) antennas are widely used in wireless fidelity (WiFi) router applications. Therefore, it is very useful to investigate which kind of diversity antenna is most suitable for current tri-band (2.4, 5.2, and 5.8 GHz) WiFi applications.

Radio propagation channels in indoor environments have been studied extensively [2–5]. The effect of electric field polarization on indoor propagation has been predicted at 1.9 GHz using a three-dimensional (3D) ray-tracing tool [4]. It has been predicted that the use of horizontally polarized (HP) dipole antennas at both the receiver and transmitter ends results in lower propagation loss than using vertically polarized (VP) dipole antennas. In Ref. [6], the performance of polarization-diversity patch antennas is compared with that of space-diversity patch antennas at 2.4 GHz in indoor environments. It was found that the use of VP space-diversity antennas at both the transmitter and receiver results in lower signal error rates in line of sight (LOS) environments, while the use of HP space-diversity antennas at both the transmitter and receiver results in better performance in non-line of sight (NLOS) environments. Polarization diversity can consistently perform under LOS and NLOS environments and is therefore more robust than space diversity. Thus far, no comprehensive comparisons have been made between different diversity antennas (including space, polarization, and pattern diversities) for wireless router applications. Compared with directional antennas, omnidirectional antennas with wider coverage are more commonly used in wireless routers. The performance of diversity antennas in different directions of the azimuthal plane should also be considered. In addition to the 2.4 GHz band, there is also a 5.0 GHz WiFi band. Since a comparison of different diversity antennas has not been carried out in this band, it is of great interest to investigate different diversity antennas in the 2.4, 5.2, and 5.8 GHz WiFi bands.

* Corresponding author.
E-mail address: eekleung@cityu.edu.hk (K.W. Leung).

https://doi.org/10.1016/j.eng.2022.09.011
2095-8099/© 2022 THE AUTHORS. Published by Elsevier LTD on behalf of Chinese Academy of Engineering and Higher Education Press Limited Company.
This is an open access article under the CC BY-NC-ND license (http://creativecommons.org/licenses/by-nc-nd/4.0/).

Polarization-diversity antennas usually employ orthogonal polarizations to obtain good isolation between their two ports. In general, there are three methods to obtain an omnidirectional polarization-diversity antenna. The first method employs multiple dual-polarized directional antennas to form a circular array [7–9]. The second method combines a VP monopole antenna and a HP omnidirectional antenna [10–15]. Both methods have the disadvantages of being large in size and complex in structure. The third method adopts two orthogonal modes in one antenna [16–18]. This method has been widely applied to single-band polarization-diversity designs. However, it has not been applied to multi-band designs due to the difficulty of obtaining multiple omnidirectional orthogonal modes at the desired frequencies. At present, the widest bandwidth of the polarization-diversity omnidirectional antenna is 78% [15] and is achieved by using the second method. However, this bandwidth is not wide enough to cover the three WiFi bands. Also, there are currently no multi-band polarization-diversity designs suitable for WiFi applications.

Usually, the coupling between the two ports of a pattern-diversity antenna is low because the two ports have different radiation patterns. In general, one of the ports has an omnidirectional radiation pattern, whereas the second port has a broadside one [19,20]. Different antenna types—including patch antennas, dielectric resonator antennas (DRAs), and dipole antennas—have been investigated for pattern-diversity designs [21–27]. Most of the designs are aimed at one frequency band, and only a few of them provide dual-band pattern diversity [22,25]. Of the existing dual-band designs, none can cover all three of the WiFi bands. Thus, it remains a challenge to design a compact pattern-diversity antenna that can completely cover the three WiFi bands.

The elements of space-diversity antennas are usually separated from one another by about half a wavelength to obtain an acceptable degree of isolation (~15 dB) [28,29]. This diversity scheme has been widely used because it is easy to design and implement. For example, space-diversity monopole antennas are common in commercial wireless routers.

The DRA has been widely investigated in past decades due to its flexible 3D structure and high efficiency [30–32]. In this paper, novel polarization- and pattern-diversity DRAs are investigated for WiFi applications. Here, glass DRAs [33] are used to increase the aesthetic appearance of the WiFi routers and thereby increase their commercial attractiveness. In designing the tri-frequency polarization-diversity DRA, a double-port feeding scheme is proposed to excite different modes of the same mode family. A stepped DRA structure is developed for tuning the targeted modes. For the tri-band pattern-diversity DRA, a staked structure is introduced to enhance the bandwidth of both the conical and the broadside radiation modes. A tri-band space-diversity DRA is also designed for the first time, and a commercial space-diversity monopole pair is used as the reference. Since it is of interest to compare the performances of the three diversity schemes, polarization-, pattern-, and space-diversity DRAs are compared with one another for the first time. Their bit error rates (BERs) are provided for a comprehensive comparison.

2. Tri-frequency polarization-diversity DRA

2.1. Antenna configuration

The configuration of the proposed tri-frequency omnidirectional polarization-diversity antenna is shown in Fig. 1. The antenna consists of a stepped cylindrical dielectric resonator (DR) and a substrate. The two stairs of the DR have different radii (r_1, r_2) and heights (h_1, h_2). At the bottom is a thin hollow region with a height of h_g = 2 mm. This small hollow region has only a small effect on the DR, but it can usefully reduce the cross-polar fields caused by the radial feeding circuit printed on the substrate. The substrate has a dielectric permittivity of ε_r, a radius of r_g, and a thickness of h_s. A coaxial probe connected to Port 1 is placed at the center to excite the DR transverse magnetic (TM) modes for vertical polarization, while arc strips are printed on the top of the substrate to excite the transverse electric (TE) modes for horizontal polarization. As illustrated in Fig. 1(b), the three groups of arc strips form three loops with respective widths of w_3, w_4, and w_5. Both the outer and inner loops are composed of four angular strips fed by a four-way power divider. The two loops are connected to Ports 2 and 3, which operate in the 2.4 and 5.0 GHz bands, respectively. In addition, the middle loop consists of eight parasitic strips to tune the mode in the 5.8 GHz band. In practical applications, a duplexer is connected to Port 1 to handle both the 2.4 and 5.0 GHz signals by using a single port.

2.2. Design methodology

Thus far, no reported omnidirectional antenna has achieved polarization diversity for the three WiFi bands. To realize tri-frequency polarization diversity in a single omnidirectional antenna, there are two challenges: ① how to excite three pairs of orthogonally polarized omnidirectional modes; and ② how to adjust each pair to the desired frequency band. This work starts with a single-band polarization-diversity design. The DR $TM_{01\delta}$ and $TE_{01\delta+1}$ modes are used in the first band, where δ refers to the field variation in the axial (z) direction ($0 < \delta < 1$). The resonant frequency of the $TM_{01\delta}$ and $TE_{01\delta+1}$ modes can be calculated by using Eqs. (1) and (2) [16]:

$$f_{TM_{01\delta}} = \frac{c}{\pi D}\sqrt{\frac{3.83^2 + \left(\frac{\pi D}{4H}\right)^2}{\varepsilon_r + 2}} \tag{1}$$

$$f_{TE_{01\delta+1}} = \frac{2.208c}{\pi D\sqrt{\varepsilon_r + 1}}\left(1.0 + 0.7013 \times \frac{D}{2H} - 2.713 \times 10^{-3}\left(\frac{D}{2H}\right)^2\right) \tag{2}$$

where f is the operating frequency, c is the speed of light in a vacuum, D is the DR diameter, and H is the DR height. When the relative permittivity ε_r of a cylindrical DRA is fixed, the DRA design has a unique diameter-to-height (D/H) ratio that gives the same operating frequency of the omnidirectional $TM_{01\delta}$ and $TE_{01\delta+1}$ modes [16]; that is,

$$f_{TM_{01\delta}} = f_{TE_{01\delta+1}} \tag{3}$$

Given the operating frequency f and ε_r, the dimensions of a cylindrical DRA are fixed. In our design, the initial dimensions of the cylindrical DRA are D = 55.70 mm and H = 24.10 mm to obtain f = 2.44 GHz and ε_r = 6.85.

Fig. 2 shows the configurations of the reference and proposed antennas. When the feeding circuits are added to the DR, the DR dimensions used in the design are slightly different from the calculated values due to the loading effect of the feeding circuits. The configuration of this basic single-band design (reference antenna I) is shown in Fig. 2(a). A short probe is placed in the center to excite the $TM_{01\delta}$ mode. To obtain a better impedance matching for this mode, a ring slot is etched on the ground plane. Four arc strips are also printed on the top of the substrate to excite the DR $TE_{01\delta+1}$ mode. The four arc strips are fed in phase by a four-way power divider. They form an electric current loop that functions as an equivalent magnetic dipole source. Fig. 3 shows the scattering (S)-parameters of the reference and proposed antennas. With reference to Fig. 3(a), each port has a resonant mode at 2.44 GHz, which fully covers the 2.4 GHz WiFi band, as expected. These two modes

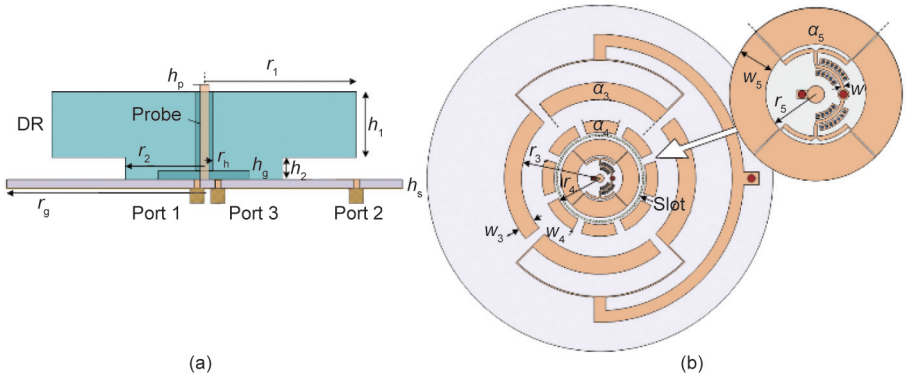

Fig. 1. Configuration of tri-frequency polarization-diversity DRA: h_1 = 15.000 mm, h_2 = 5.000 mm, h_s = 1.524 mm, r_1 = 34.800 mm, r_2 = 18.000 mm, r_3 = 20.100 mm, r_4 = 11.800 mm, r_5 = 5.800 mm, α_3 = 84.000°, α_4 = 35.500°, α_5 = 89.000°, w_3 = 4.400 mm, w_4 = 3.000 mm, w_5 = 4.200 mm, r_h = 2.000 mm, h_p = 23.500 mm, h_g = 2.000 mm, w = 0.500 mm, and r_g = 50.000 mm. (a) Side view; (b) feeding circuits. DR: dielectric resonator; r_1, r_2: the radius of DR; r_3, r_4, and r_5,: the radius of the feeding loops; h_1, h_2: the height of DR; h_g: the height of the hollow region; h_p: the height of the coaxial probe; ε_r: dielectric permittivity; r_g: the radius of the substrate; r_h: the radius of the hole in DR; h_s: the thickness of the substrate; w_3, w_4, and w_5: the widths of the feeding loops; α_3, α_4, and α_5: the arc angles of the feeding loops; w: the width of the feeding line. The width of the slot (g) is 0.5 mm.

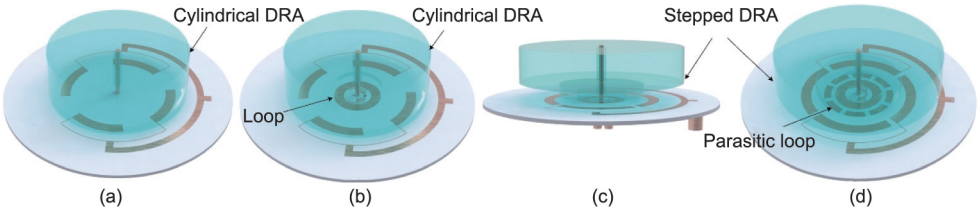

Fig. 2. Configurations of the reference and proposed antennas. (a) Reference antenna I; (b) proposed reference antenna II; (c) proposed reference antenna III; (d) proposed polarization-diversity antenna.

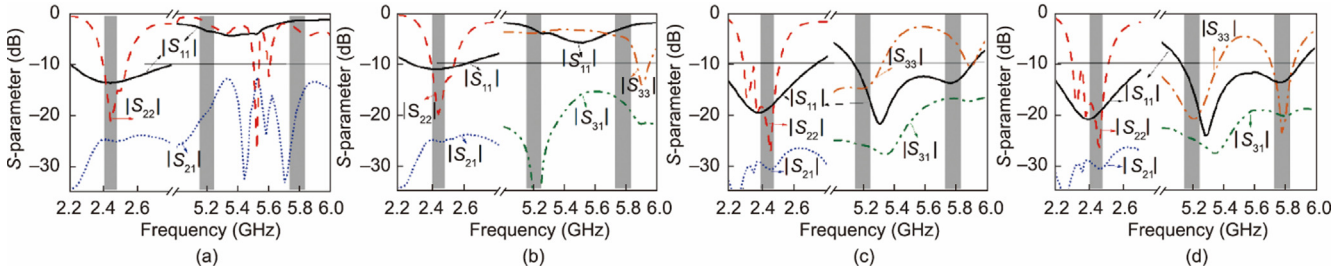

Fig. 3. Simulated reflection coefficients of the reference and proposed antennas. (a) Reference antenna I; (b) proposed reference antenna II; (c) proposed reference antenna III; (d) proposed polarization-diversity antenna. *S*: scattering.

are $TM_{01\delta}$ and $TE_{01\delta+1}$ with good omnidirectional radiation fields. However, there is no resonant mode at the desired 5.2/5.8 GHz band. Port 1 has a weak resonant mode at about 5.5 GHz, while Port 2 has two resonances at 5.5 and 5.6 GHz. Fig. 4(a) shows the electric (E)-field distribution and radiation pattern of Port 2 at 5.5 GHz. The E-field distribution is consistent with that of the $HEM_{41\delta+3}$ mode. Its azimuth (ϕ) component of electric field (E_ϕ) has an azimuthal variation, leading to large ripples in the horizontal plane and thus to an irregular radiation pattern. The other resonant mode in the 5 GHz band was also examined, and similar results were obtained. This irregular radiation pattern is not desirable for the omnidirectional coverage of WiFi applications.

To obtain HP omnidirectional fields in the 5 GHz band, the higher order modes of the TE mode family were considered. If the E-field of a mode has no variation in E_ϕ, the DRA will radiate omnidirectionally in the horizontal plane. Therefore, the higher order mode in the ϕ direction of cylindrical coordinates is not omnidirectional, and only the higher order modes in the radial and z directions can be used. As it is not easy to manipulate z direction higher order modes when the DR dimensions are fixed, we focus on these at the radial direction. A potential higher order mode is shown in Fig. 4(b). Its E-field distribution has a circular region at the center and a concentric ring in the outer region. The fields in the two regions are out of phase. In each region, the E-field distribution along the ϕ direction is uniform and in phase, with no azimuthal variations. To excite this mode, a small electric current loop fed by another port (Port 3) is required at the bottom of the DR. The antenna configuration (proposed reference antenna II) is shown in Fig. 2(b), and its *S*-parameters are illustrated in Fig. 3 (b). It can be seen from Fig. 3(b) that a resonant mode is excited at 5.9 GHz for Port 3, which is the $TE_{02\delta+3}$ mode, as expected. Although it is a higher order mode, it has been able to confirm that the radiation pattern is omnidirectional in the horizontal x–y plane. This can be verified by the simulated radiation pattern, as

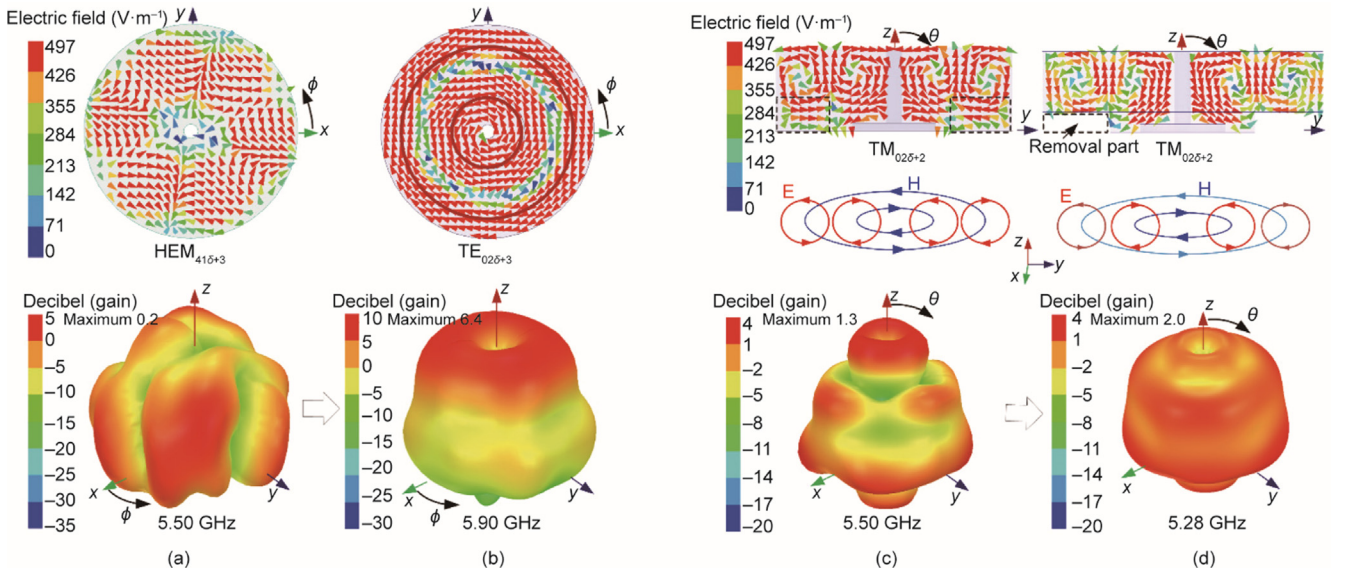

Fig. 4. Simulated electric (E)-field distributions and 3D radiation patterns of the reference antennas, showing the evolution of radiation patterns. (a) Reference antenna I in the $HEM_{41\delta+3}$ mode; (b) proposed reference antenna II in the $TE_{02\delta+3}$ mode; (c) proposed reference antenna II in the $TM_{02\delta+2}$ mode; (d) proposed reference antenna III in the $TM_{02\delta+2}$ mode. HEM: hybrid electromagnetic mode; ϕ: azimuth; θ: elevation; E: electric; H: magnetic.

shown in Fig. 4(b). The tilted angle of the radiation pattern is due to the increasing electrical size of the ground plane with increasing frequency. Although the omnidirectional TE mode is excited, its resonant frequency is not at the desired band, nor does it coincide with that of the TM mode. On the other hand, the size of the DR cannot be adjusted too far from the original values to maintain the 2.4 GHz diversity design. Therefore, it is almost impossible to obtain a dual-frequency polarization-diversity DRA for WiFi applications by using a conventional DR, not to mention obtaining a tri-frequency design.

Since the E-field distributions of the higher order modes used in this design are different from those of the fundamental modes in the radial and z directions, a stepped DRA is proposed in order to obtain higher degrees in the two dimensions. The resonant frequencies and radiation patterns in the vertical plane of these higher order modes can be adjusted by tuning the E-field distribution along the radial direction. Fig. 2(c) shows the stepped DRA (proposed reference antenna III), in which the same material is used for the two layers. By using a smaller bottom layer and a larger top layer, the 2.4 GHz resonant modes can be maintained, as shown in Fig. 3(c). In addition, for the VP Port 1, the 5.5 GHz $TM_{02\delta+2}$ mode of antenna II is tuned to 5.28 GHz in antenna III, covering the 5.2 GHz WiFi band. With reference to Fig. 4(c), the sideview of the E-field distributions has four loops in the y–z plane: two on the left hand side and two on the right hand side. It is known that the electric (E) and magnetic (H) fields are perpendicular to each other, and the H-field is strongest when the E-field is weakest in the resonant DR. In the x–y plane, the induced H-field shows two out-of-phase concentric loops, which are perpendicular to the E-field loops. No variations of the azimuth component of magnetic field (H_ϕ) are found in the H-field distribution; therefore, the radiation associated with the two H-field loops is omnidirectional in the horizontal x–y plane. This can be verified by the simulated radiation pattern, as shown in Fig. 4(c). Nevertheless, it can be seen from the figure that the radiation does not concentrate in the desired direction ($30° \leq \theta \leq 90°$, where θ is the elevation angle relative to the z-axis). To tune the beam in the vertical plane, part of the radiator where the outer E-field loops are located is removed, as shown in Fig. 4(d). In this case, the outer E-field loops near the sidewall of the DR are weakened; therefore, their induced (outer) H-field loop also becomes weaker. As a result, the two H-field loops have net radiation, and this radiation in the vertical plane can be tuned by changing the removal part of the radiator. As for the HP Port 3, it is found that a higher order $TE_{03\delta+1}$ mode with a good omnidirectional radiation pattern is excited at 5.23 GHz, forming polarization diversity with the $TM_{02\delta+2}$ mode of Port 1 in the 5.2 GHz band. In addition, a resonant mode is generated at 5.8 GHz for the VP Port 1, which is due to the feeding probe.

However, it can be noted from Fig. 3(c) that the 5.9 GHz $TE_{02\delta+3}$ mode deviates from the 5.8 GHz band. To tune the 5.9 GHz mode independently, a parasitic loop is introduced close to the small inner loop, as illustrated in Fig. 2(d) (proposed antenna). It can be observed from Fig. 3(d) that the $TE_{02\delta+3}$ mode is successfully tuned to 5.8 GHz, overlapped with the probe mode. Its radiation pattern is also improved by the parasitic strip, showing a wider beam width. Thus, polarization diversity is obtained at the 5.8 GHz band. To characterize the DR modes of the proposed antenna, their E-field patterns are presented in Fig. 5. It can be observed that five modes are excited in one DR at the desired bands.

To facilitate the multi-band diversity DRA design, a design guideline is summarized as follows:

(1) Analyze the radiation requirement of the antenna, and then determine two operating DRA modes for the 2.4 GHz band.

(2) Determine the dimensions of the DRA so that the two DRA modes operate in the same frequency band.

(3) Design the feeding circuits for the two DRA modes. From the field distribution, find suitable higher order modes that are close to the upper bands.

(4) Deploy loading techniques (e.g., a special DRA shape, combination of different materials, feeding circuits at proper positions, etc.) to shift the higher order modes to the upper bands.

(5) Finally, optimize the impedance matching and radiation patterns for all the bands.

2.3. Measurement verification

A prototype of the proposed tri-frequency polarization-diversity antenna was fabricated and measured to verify the design. The DR was fabricated with K9 glass (ε_r = 6.8500,

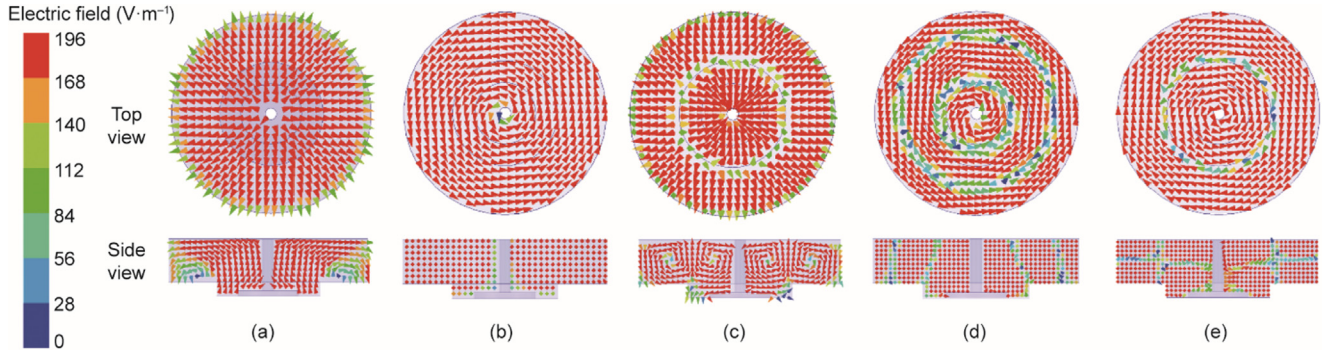

Fig. 5. Simulated E-field distribution of the proposed polarization-diversity DRA. (a) $TM_{01\delta}$ at 2.44 GHz; (b) $TE_{01\delta+1}$ at 2.44 GHz; (c) $TM_{02\delta+2}$ at 5.28 GHz; (d) $TE_{03\delta+1}$ at 5.20 GHz; (e) $TE_{02\delta+3}$ at 5.80 GHz.

tanδ = 0.0100), while the feeding circuits were printed on a substrate with a dielectric constant of ε_r = 3.5500 and a loss tangent of tanδ = 0.0027. Two photos of the prototype are shown in Fig. 6. In this paper, a four-port network analyzer E5071C (Agilent Technologies, Inc., USA) was used to measure the reflection coefficients, while a Satimo StarLab system (MVG, France) was used to obtain the radiation pattern and antenna gains.

Fig. 7 presents the simulated and measured *S*-parameters, antenna gains, total efficiencies, and envelope correlation coefficients (ECCs). It can be seen that a reasonable agreement is obtained between the simulated and measured results. With reference to Fig. 7(a), the measured −10 dB impedance passbands for the VP Port 1 are 2.20–2.70 and 5.05–5.86 GHz. For the HP ports, the measured passband is 2.38–2.50 GHz for Port 2, and 4.90–5.27 and 5.60–5.85 GHz for Port 3. The overlapped bandwidths are 4.90% (2.38–2.50), 4.26% (5.05–5.27), and 4.36% (5.60–5.85), fully covering the three WiFi bands. Among the three pairs of modes with orthogonal polarizations, there are five DR modes and one probe mode, and the port isolations are as high as 30, 25, and 20 dB for the three bands. It can be seen from Fig. 7(b) that the measured VP antenna gains at (ϕ = 0°, θ = 60°) for Port 1 are 1.0, 0.3, and 1.3 dBi in the 2.4, 5.2, and 5.8 GHz bands, respectively. The measured HP gain in this direction is 3 dBi in the 2.40 GHz band for Port 2, whereas the HP gains are 2.00 and −0.75 dBi in the 5.20 and 5.80 GHz bands for Port 3. In the 5.8 GHz band, the maximum gain direction is changed from θ = 60° to 30° because of the tilting-angle effect caused by the increased electrical size of the ground plane (the maximum gain is ~6 dBi at around 30° in this band). As can be seen in Fig. 7(c), the total antenna efficiencies of the VP Port 1 are 93%, 77%, and 72%, respectively, at the three bands, taking impedance matching into account. For the HP Ports 2 and 3, the respective efficiencies of the three bands are 80%, 73%, and 70%. The antenna efficiency of the 5 GHz band is generally lower than that of the 2.4 GHz band. This is reasonable, because the loss caused by the glass increases with frequency. As shown in Fig. 7(c), the efficiency can be significantly improved by using glass with a lower dielectric loss tangent. The ECCs of the DRA, a performance index for a MIMO antenna, are illustrated in Fig. 7(d). Our simulated and measured ECCs were obtained by using Eq. (4) [16,34]:

$$\rho_e = \frac{\left|\int\int_{4\pi}\left[\mathrm{XPR}\cdot E_{\theta 1}(\Omega)\cdot E^*_{\theta 2}(\Omega)\cdot P_\theta(\Omega)+E_{\phi 1}(\Omega)\cdot E^*_{\phi 2}(\Omega)\cdot P_\phi(\Omega)\right]\mathrm{d}\Omega\right|^2}{\int\int_{4\pi}\mathrm{XPR}\cdot G_{\theta 1}(\Omega)\cdot P_\theta(\Omega)+G_{\phi 1}(\Omega)\cdot P_\phi(\Omega)\mathrm{d}\Omega\cdot\int\int_{4\pi}\mathrm{XPR}\cdot G_{\theta 2}(\Omega)\cdot P_\theta(\Omega)+G_{\phi 2}(\Omega)\cdot P_\phi(\Omega)\mathrm{d}\Omega} \tag{4}$$

where ρ_e is the value of ECC, E_θ is the θ-polarized active electric field patterns of the antennas when both ports are excited, E_θ* is the conjugation of E_θ. In Eq. (4), XPR is the cross-polarization power ratio of the incident waves. It is set to 1 to model a uniform propagation environment [16]. G_θ and G_ϕ are the θ- and ϕ-polarized components of the active power gain patterns of the antenna. The symbol Ω denotes the solid angle, and P_θ and P_ϕ denote the θ- and ϕ-components of the angular power density functions of the incoming plane wave, respectively. P_θ and P_ϕ can be statistically modeled with a Gaussian distribution in the elevation plane and a uniform distribution in the azimuthal plane for the angular power density functions [16,34], respectively. The ECCs between different polarized ports are lower than −20.0, −28.0, and −18.0 dB for the 2.4, 5.2, and 5.8 GHz bands, respectively. Due to the orthogonal polarization, it is desirable for them to be much lower than the criteria of −3 dB.

The simulated and measured normalized radiation patterns at 2.44, 5.20, and 5.80 GHz are shown in Fig. 8. At the elevation plane (ϕ = 0°), a null is observed in the *z*-axis direction (θ = 0°), which is desirable for conical radiation patterns. At the θ = 60° plane, the cross-polar fields are generally lower than the co-polar fields by 17 dB. Although the radiation patterns in the three bands are not the same, they can still provide efficient and uniform signal coverage in the horizontal plane for end users.

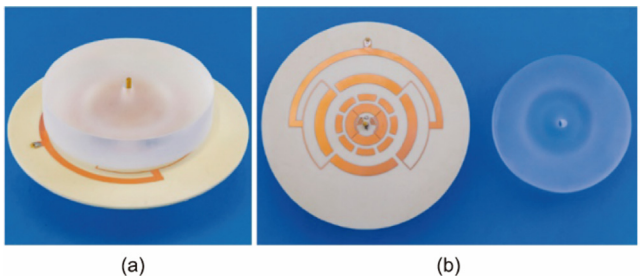

Fig. 6. Photos showing the tri-frequency polarization-diversity DRA prototype. (a) Perspective view; (b) feeding circuit and DR.

3. Tri-band pattern-diversity DRA

3.1. Antenna configuration

Fig. 9 presents the configuration of the proposed tri-band pattern-diversity DRA, which consists of a stacked cylindrical DR of two dielectric layers and a substrate. The two dielectric layers of the DR have different radii (r_1, r_2), heights (h_1, h_2), and dielectric constants (ε_{r_1}, ε_{r_2}). The substrate has a dielectric permittivity of ε_r and a thickness of h_s. A circular ground plane is printed on the substrate, and a rectangular slot and probe are used to excite the broadside and conical radiation modes of the DR, creating pattern diversity. The slot and probe are fed by grounded coplanar waveguide (GCPW) lines, which can reduce the cross-polarized fields.

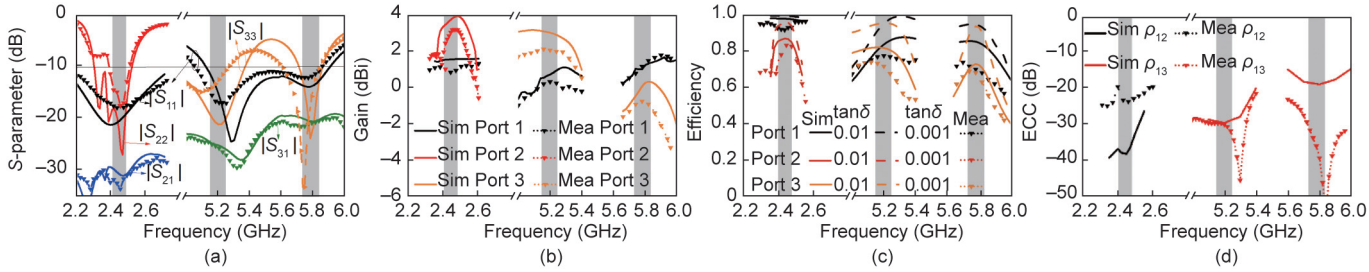

Fig. 7. Measured and simulated S-parameters, antenna gains, efficiencies, and ECCs of the tri-frequency polarization-diversity DRA prototype. (a) *S*-parameters; (b) antenna gains at (ϕ = 0°, θ = 60°); (c) total efficiencies; (d) ECCs. Sim: simulated; Mea: measured.

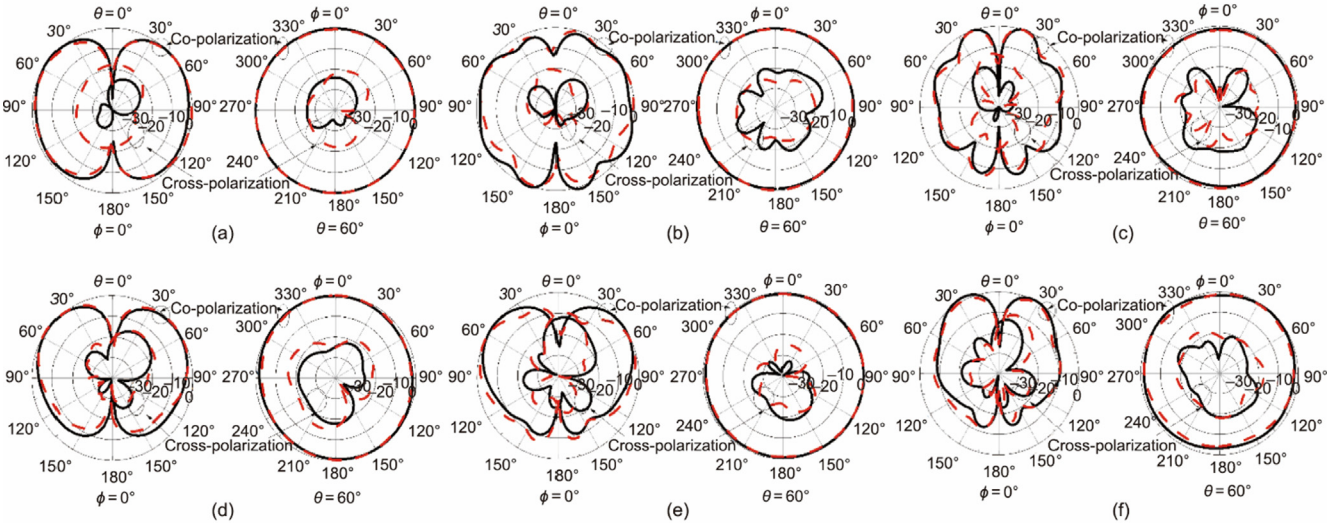

Fig. 8. Measured and simulated normalized radiation patterns of the tri-frequency polarization-diversity DRA prototype (black solid line: simulated; red dashed line: measured). (a–c) VP Port 1 at 2.44, 5.20, and 5.80 GHz; (d) HP Port 2 at 2.44 GHz; (e, f) HP Port 3 at 5.20 and 5.80 GHz.

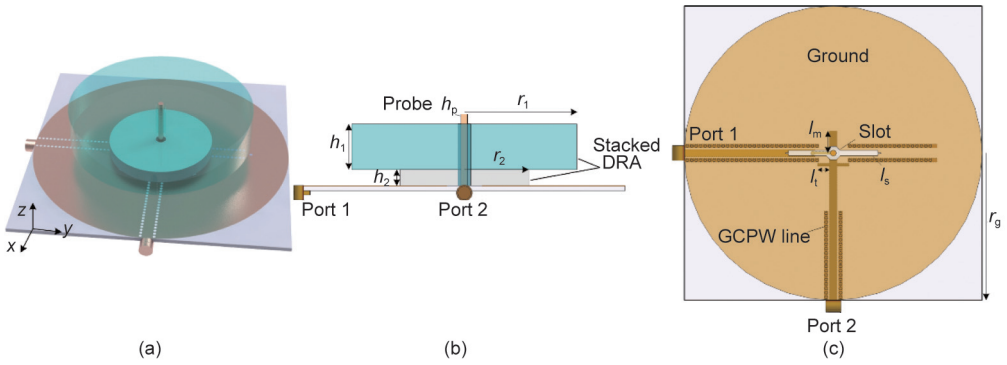

Fig. 9. Configuration of tri-band pattern-diversity antenna: r_1 = 35.000 mm, r_2 = 20.000 mm, h_1 = 14.000 mm, h_2 = 5.000 mm, l_s = 32.000 mm, l_m = 7.500 mm, l_t = 5.250 mm, h_p = 22.000 mm, and r_g = 50.000 mm. (a) Perspective view; (b) side view; (c) ground plane. GCPW: grounded coplanar waveguide; l_s: length of slot; l_m: stub length of microstrip line; l_t: length of open stub; The width of the slot is 1.800 mm the width of the open stub is 1.000 mm, the radius of the probe is 2.000 mm, the thickness of the substrate is 1.524 mm, and the dielectric constants of the two dielectric layers of the DR are ε_{r_1} = 6.850 and ε_{r_2} = 3.000.

3.2. Design methodology

Dual-band pattern-diversity antennas usually have a narrow bandwidth in their upper band, as a higher order mode of the radiator or a resonant mode of the feeding circuit is commonly used for the upper band. Therefore, they cannot simultaneously support the three bands (2.4, 5.2, and 5.8 GHz) of WiFi applications. There are two potential solutions for a pattern-diversity design to cover all three WiFi bands. One solution is to manipulate three pairs of modes with broadside/conical radiation patterns to the three desired bands, respectively. The other is to design a dual-band pattern-diversity antenna with a wide upper band that can cover both the 5.2 and 5.8 GHz bands. Since it is not easy to implement the individual tuning of three pairs of resonant modes in one resonator, we use the latter method in our pattern-diversity design.

According to the design guideline in Section 2.2, the pattern-diversity antenna is developed step by step. It is known from the polarization-diversity DRA in Section 2 that two TM modes can

be obtained in the 2.4/5.2 GHz bands by using a stepped DRA. Therefore, a stepped structure is also employed in this pattern-diversity design, in which only one kind of material is used for the DR. A slot is also introduced in the center of the ground plane to excite broadside radiation patterns. The configuration and *S*-parameters of this reference antenna IV are shown in Figs. 10(a) and (b). It can be observed from the figure that, at the 2.40 GHz band, two resonant modes are excited at 2.25 and 2.52 GHz for Port 1, caused by the DR loaded probe mode and the DR $TM_{01\delta}$ mode. A resonant mode for Port 2 is found at 2.45 GHz, which is the $HEM_{11\delta}$ mode. With reference to the 5 GHz band, both ports have one resonant mode, which is not sufficient to cover both the 5.2 and 5.8 GHz bands.

Inspired by wideband stacked DRAs with broadside radiation patterns [35], a stacked structure with two different materials is adopted in our stepped DRA. As shown in Fig. 10(c), a larger cylindrical DR with a higher dielectric constant ε_{r_1} is stacked on a smaller cylindrical DR with a lower constant ε_{r_2}. The *S*-parameters of this proposed antenna are shown in Fig. 10(d). In the first band, the two modes of Port 1 shift upward and merge at 2.60 GHz, while the mode of Port 2 shifts to 2.54 GHz. However, the modes can still cover the 2.4 GHz WiFi band. In regard to the 5.0 GHz band, both ports obtain wider bandwidths compared with reference antenna IV and can now simultaneously cover the 5.2/5.8 GHz WiFi bands. Due to the stacked DRA, the bandwidth of the $HEM_{12\delta+3}$ mode, which dominates in the 5 GHz band for Port 2, is broadened as expected. Also, the bandwidth of the $TM_{02\delta+2}$ mode is effectively enhanced for Port 1.

3.3. Measurement verification

Fig. 11 shows photos of the proposed tri-band pattern-diversity antenna prototype. The materials used in this prototype were the same as those used for the polarization-diversity design, except for a dielectric material with $\varepsilon_{r_2} = 3$.

The simulated and measured *S*-parameters, antenna gains, total efficiencies, and ECCs are shown in Fig. 12. Reasonable agreement is obtained between the simulated and measured results. It can be seen from Fig. 12(a) that the measured overlapped bandwidths of the two ports are 16% (2.30–2.70) and 17% (5.04–5.98), fully covering the 2.40, 5.20, and 5.80 GHz WiFi bands. In addition, the two ports have high isolations of 23.5, 22.5, and 21.0 dB for the three WiFi bands. Fig. 12(b) shows the measured and simulated antenna gains. The measured antenna gains at ($\phi = 0°$, $\theta = 60°$) for the omni-directional Port 1 are 0.06, 0.96, and 0 dBi at the 2.40, 5.20, and 5.80 GHz bands, respectively. For Port 2, with broadside radiation patterns, the measured boresight gain is 6.8, 11.4, and 4.0 dBi in the three bands. The large gain discrepancy between 5.2 and 5.8 GHz occurs because the higher order DRA mode is disturbed by the resonance of the feeding slot at 5.8 GHz. This problem can be mitigated by using a larger ground plane. It was found that, by increasing the ground plane size from r_g = 50.0 to 65.0 mm, the simulated antenna gain at 5.8 GHz increased from 5.0 to 9.4 dBi, with only a small effect on the other bands. As can be determined from Fig. 12(c), the total antenna efficiencies of Port 1 are 82%, 77%, and 72% in the three bands, while they are 85%, 79%, and 78% for Port 2. The ECCs obtained from the radiation patterns are illustrated in Fig. 12(d). Both the simulated and measured ECCs between the two ports are lower than −20.0, −18.5, and −15.0 dB for the 2.4, 5.2, and 5.8 GHz bands, respectively, and are much lower than the criteria of −3.0 dB due to the different patterns of the two ports.

Fig. 13 presents the simulated and measured normalized radiation patterns at 2.44, 5.20, and 5.80 GHz. At the elevation plane ($\phi = 0°$), a null is found in the *z*-axis direction ($\theta = 0°$) for Port 1, which is typical for conical radiation patterns. In contrast, the radiation patterns of Port 2 show a peak in the *z*-axis direction, which leads to high isolation between the two ports.

4. Tri-band space-diversity antennas

To facilitate the comparison of different diversity antennas, a space-diversity DRA for the three WiFi bands was also designed.

4.1. Antenna configuration

Fig. 14 shows the configuration of the single glass DRA and its fabricated prototype. With reference to Fig. 14(a), the DR is fed by a long probe, excited at the $TM_{01\delta}$, $TM_{01\delta+2}$, and $TM_{01\delta+4}$ modes at 2.40, 5.05, and 5.75 GHz, respectively. A ring slot is introduced on the ground plane to mitigate the tilting angle of the radiation patterns in the 5 GHz band. Fig. 14(c) shows a photo of the fabricated single DRA prototype.

4.2. Measurement verification

The radiation patterns of the single antenna at 2.44, 5.20, and 5.80 GHz are shown in Fig. 15. It can be observed that symmetrical radiation patterns are obtained at the three frequencies. At the plane of $\theta = 60°$, the cross-polarized fields are generally weaker than their co-polarized counterparts by 17 dB.

Two glass DRAs with a center-to-center distance of *d* are used to form a space-diversity DRA, as shown in Fig. 16(a). Different space values (*d*) from $0.4\lambda_0$ to $0.7\lambda_0$ were studied, where λ_0 is the wavelength in a vacuum at 2.44 GHz. It was found that the isolation in the 5 GHz band is generally higher than 20 dB for different *d*. Thus, the effect of *d* is more obvious in the 2.4 GHz band. Further increasing the space results in a smaller improvement. Similarly, using a larger *d* will weaken the undesirable effect of interference on the radiation pattern. As a compromise between antenna size and performance, $0.5\lambda_0$ was chosen in our design. The measured and simulated *S*-parameters, antenna gains, efficiencies, and ECCs are shown in Figs. 16(b)–(d). As shown in Fig. 16(b), three resonant modes are obtained at 2.4, 5.1, and 5.8 GHz, forming wide

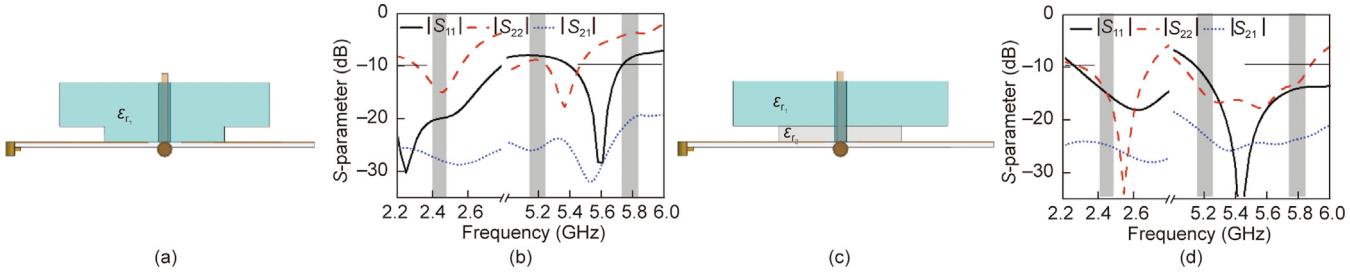

Fig. 10. Configurations and *S*-parameters of the reference and proposed antennas. (a) Configuration of reference antenna IV; (b) *S*-parameters of reference antenna IV; (c) configuration of the proposed pattern-diversity DRA; (d) *S*-parameters of the proposed pattern-diversity DRA.

Fig. 11. Photos of the tri-band pattern-diversity DRA prototype. (a) Perspective view; (b) DR and feeding circuit.

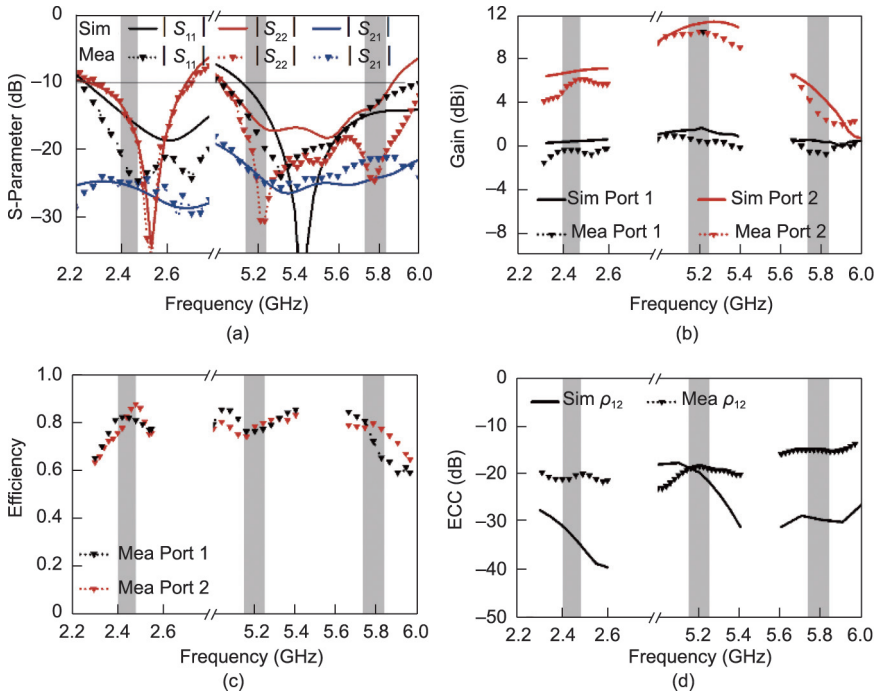

Fig. 12. Measured and simulated S-parameters, antenna gains, efficiencies, and ECCs of the tri-band pattern-diversity DRA prototype. (a) *S*-parameters; (b) antenna gains at (ϕ = 0°, θ = 60°) for Port 1 and (θ = 0°) for Port 2; (c) total efficiencies; (d) ECCs.

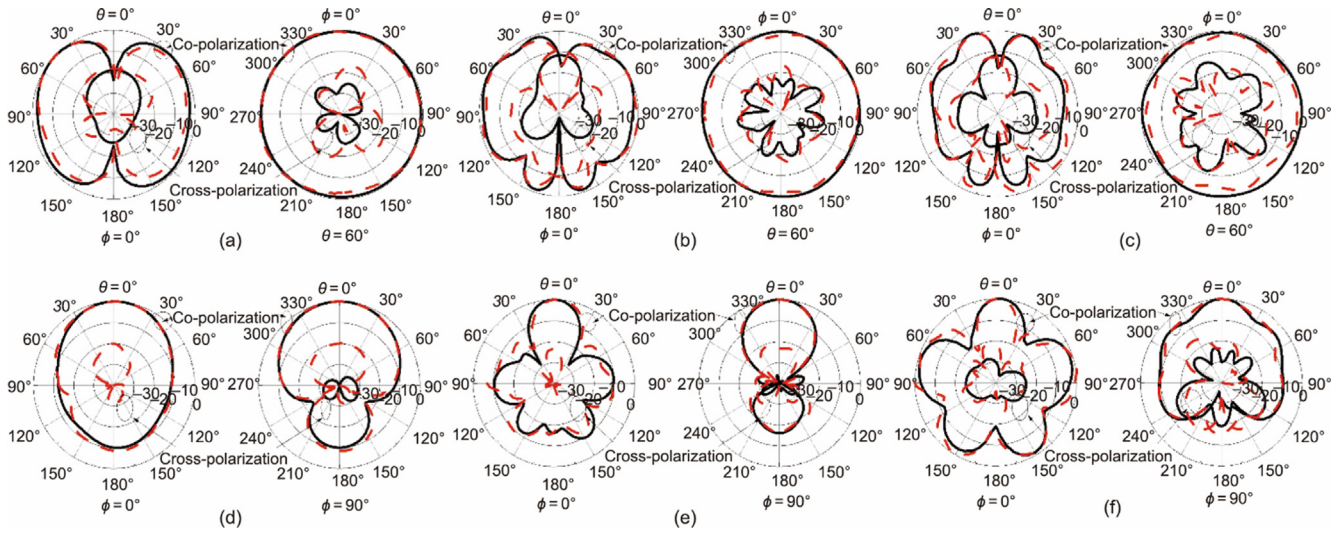

Fig. 13. Measured and simulated normalized radiation patterns of the tri-band pattern-diversity DRA prototype (black solid line: simulated; red dashed line: measured). (a–c) Port 1 at 2.44, 5.20, and 5.80 GHz; (d–f) Port 2 at 2.44, 5.20, and 5.80 GHz.

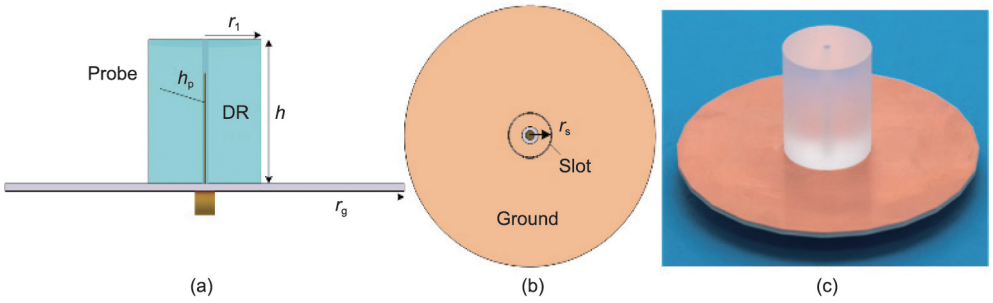

Fig. 14. Configuration of the tri-band single DRA and a photo of its prototype: r_1 = 13.000 mm, h = 32.500 mm, h_p = 23.500 mm, r_s = 7.500 mm, and r_g = 45.000 mm. (a) Side view; (b) ground plane; (c) photo of the prototype. h: height of DRA. r_p is 0.450 mm, g is 0.500 mm, h_s is 1.524 mm, and ε_r is 3.550.

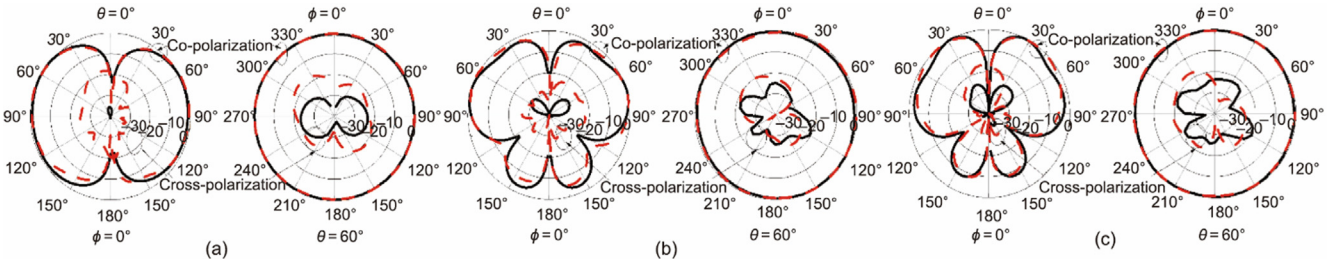

Fig. 15. Measured and simulated normalized radiation patterns of the tri-band single DRA prototype (black solid line: simulated; red dashed line: measured). (a) 2.44 GHz; (b) 5.20 GHz; (c) 5.80 GHz.

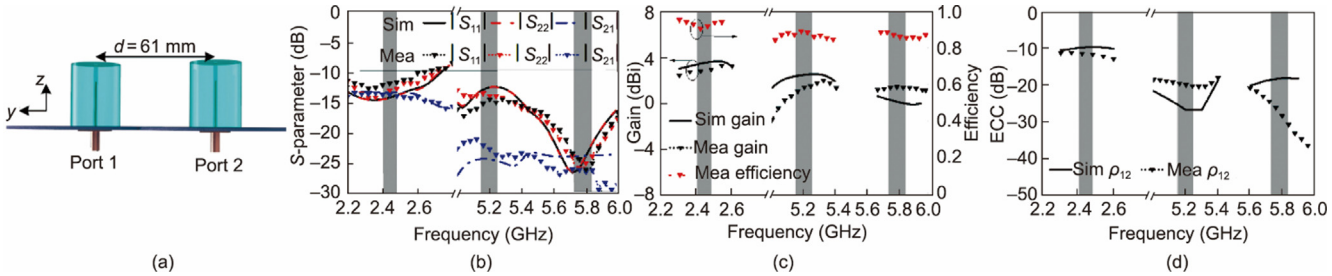

Fig. 16. Measured and simulated *S*-parameters, antenna gains, efficiencies, and ECCs of the proposed tri-band space-diversity DRA prototype. (a) Configuration; (b) *S*-parameters; (c) antenna gains at (ϕ = 0°, θ = 60°) and total efficiencies for Port 1; (d) ECC.

bandwidths that can cover the entire 2.4 and 5.0 GHz bands. The measured isolations between the two ports of the space-diversity DRA are 14.0, 22.0, and 26.0 dB in the 2.4, 5.2, and 5.8 GHz bands, respectively. Fig. 16(c) presents the measured and simulated antenna gains and efficiencies. The measured antenna gains at (ϕ = 0°, θ = 60°) for Port 1 are 2.7, 1.3, and 1.3 dBi in the three bands. High efficiencies of 90%, 88%, and 86% are also obtained within the three bands. As shown in Fig. 16(d), the measured ECCs are −11.5, −20.0, and −27.0 dB in the three bands, due to the increased separation distance with increased frequency.

The simulated and measured normalized radiation patterns of Port 1 at 2.44, 5.20, and 5.80 GHz are shown in Fig. 17. At the elevation plane (ϕ = 0°), the radiation patterns are not as symmetrical as those of the single antenna. This is reasonable, because some fields are disturbed by the adjacent DRA, leading to a gain variation at the (θ = 60°) plane.

4.3. Measurement of space-diversity commercial monopoles

To benchmark the performance of the proposed glass DRAs, two commercial monopoles with a distance of d = 61 mm (0.5λ_0 at 2.44 GHz), forming space diversity, were also measured as a reference. A photo of the monopoles is provided in Fig. 18(a). The measured *S*-parameters, antenna gains, efficiencies, and ECC obtained from the measured radiation patterns are illustrated in Figs. 18(b)–(d). With reference to Fig. 18(b), the measured −10 dB impedance passbands are 2.22–2.54, 5.14–5.32, and 5.48–6.00 GHz, fully covering the three WiFi bands. The isolations between the two ports are also shown in the figure, at 14.5, 24.5, and 24.6 dB. Within the three bands, the measured antenna gains are 0, 0.50, and 0.35 dBi. Relatively low efficiencies of 67%, 64%, and 60% are observed. It can be seen from Fig. 18(d) that the ECCs of the space-diversity monopoles are −13.6, −21.8, and −23.0 dB, which are comparable with those of the space-diversity DRA.

Fig. 19 shows the measured radiation patterns of the space-diversity monopoles. The measured radiation patterns are more symmetrical and uniform compared with those of the space-diversity DRA. This is because the monopole is thinner, resulting in fewer reflected fields.

5. Comparison of diversity antennas

The four diversity antennas described above have comparable antenna gains around θ = 60°in their conical beams. With reference

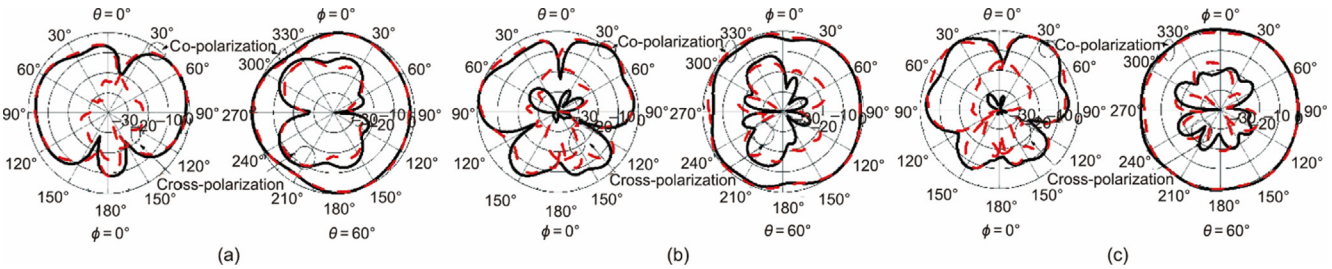

Fig. 17. Simulated and measured normalized radiation patterns of the proposed tri-band space-diversity DRA prototype (black solid line: simulated; red dashed line: measured). (a) 2.44 GHz; (b) 5.20 GHz; (c) 5.80 GHz.

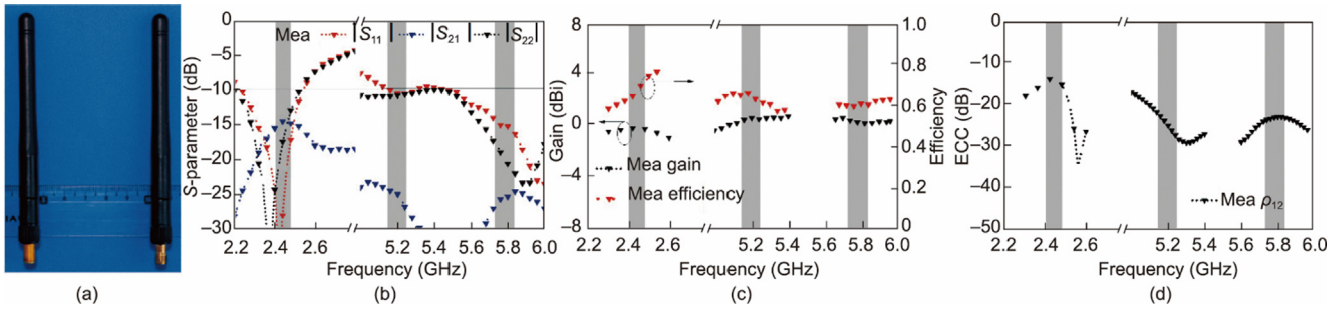

Fig. 18. Photo of a commercial space-diversity monopole pair and its measured *S*-parameters, antenna gains, efficiencies, and ECCs. (a) Photo of space-diversity monopoles; (b) *S*-parameters; (c) antenna gains at (ϕ = 0°, θ = 60°) and total efficiencies for Port 1; (d) ECC.

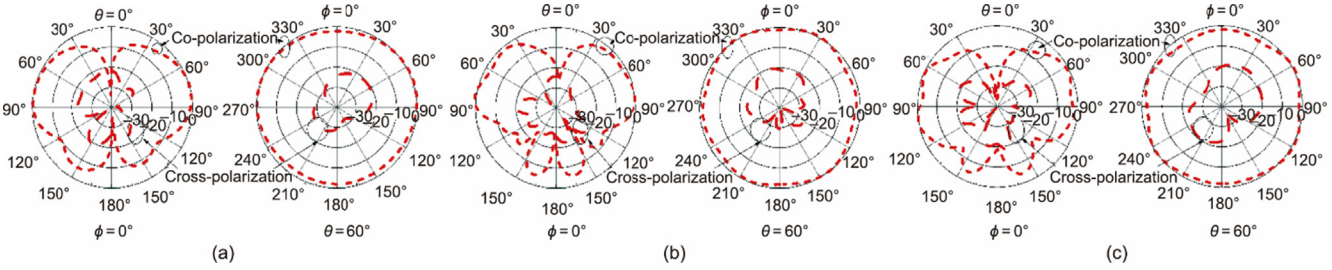

Fig. 19. Measured normalized radiation patterns of the commercial space-diversity monopole antennas. (a) 2.44 GHz; (b) 5.20 GHz; (c) 5.80 GHz.

to the antenna efficiencies, the space-diversity monopoles have relatively low efficiencies of 60%–67%. The other three diversity antennas have efficiencies of 70%–90%. To provide a more comprehensive comparison, the BER of the four diversity antennas were measured using a 2T2R MIMO system composed of a PXIe Chassis M9018B Advanced Switch Fabric (Keysight Technologies, Inc., USA) and a DSO-X 91604A Oscilloscope (Agilent Technologies, Inc., USA). To avoid the time-varying background noise in a real environment, our BER measurements were done in an anechoic chamber. As the antennas under test (AUT) have omnidirectional radiation fields, they were rotated 90° after the measurement of each direction. Thus, four directions (ϕ = 0°, 90°, 180°, and 270°) were considered in our measurement to check the radiation uniformity of the diversity antennas. In the measurement, the four diversity antennas for tri-band WiFi routers were used as the receiver, while a diversity antenna consisting of two monopoles was used as the transmitter. To provide a comprehensive comparison, all three fundamental end-user cases were considered in our chamber measurements: namely, the case of two vertical (VV) monopoles, the case of one vertical monopole and one horizontal (VH) monopole, and the case of two horizontal (HH) monopoles. Other variant cases can be regarded as a partial superposition of the three cases and are therefore not included here for brevity. If a Rayleigh environment is used, the polarization of the incident wave could be altered, and the VV and HH cases may have stronger cross-polar fields. In that case, the BER could be close to that of the VH case.

Fig. 20 shows the experimental setup of the 2T2R MIMO system using the WLAN 802.11ac protocol for the BER test. The different diversity antennas can also be used in the WLAN 802.11ax (WiFi

Fig. 20. Photographs showing the measurement setup. (a) Measurement scheme; (b) transmit and receive antennas. TX: transmitting; RX: receiving; AUT: antennas under test.

6) protocol. For the 802.11ac protocol, the ideal data rate can be obtained as follows:

$$\text{Date rate} = N_{SD} \times N_{BPSCS} \times R \times N_{SS}/(T_{DFT} + T_{GI}) \quad (5)$$

where the symbols are defined as follows (the bracket shows the value of the parameter used in the experiment):

N_{SD}: number of data subcarriers (N_{SD} = 52),

N_{BPSCS}: number of coded bits per subcarrier per stream (N_{BPSCS} = 4),

R: coding (R = 3/4),

N_{SS}: number of spatial streams (N_{SS} = 2),

T_{DFT}: OFDM symbol duration (T_{DFT} = 3.2 μs),

T_{GI}: guard interval duration (T_{GI} = 0.8 μs).

By using these values for the parameters in the SystemVue software (Keysight Technologies, Inc., USA) for Keysight test equipment, the data rate is 78 Mb·s^{-1}. When the BER > 0, the real data rate can be obtained using the formula:

$$\text{Real date rate} = \text{Date rate} \times (1 - \text{BER})^{B_{PF}} \quad (6)$$

where B_{PF} (bits per frame) is 100 in our experimental setting.

Fig. 21 shows the measured BERs at 2.44, 5.20, and 5.80 GHz. It can be observed from Fig. 21(a) that, when both the transmitting monopoles are VP (the VV case) at 2.44 GHz, the space-diversity DRA that has the same polarization as the transmitting antennas requires the lowest input power to obtain a BER of less than 1%. However, the space-diversity DRA's performance varies greatly in different directions. To keep the BER within 1%, the required power of the polarization-diversity DRA is a little larger than that of the space-diversity DRA, which is reasonable, because one port of the polarization-diversity DRA has a different polarization from the transmitting antennas. Nevertheless, stable performances are observed across different directions for the polarization-diversity DRA. For the two transmitting antennas in the VH and HH cases, the polarization-diversity DRA requires the lowest input power to keep its BER at less than 1% and remains the most stable across

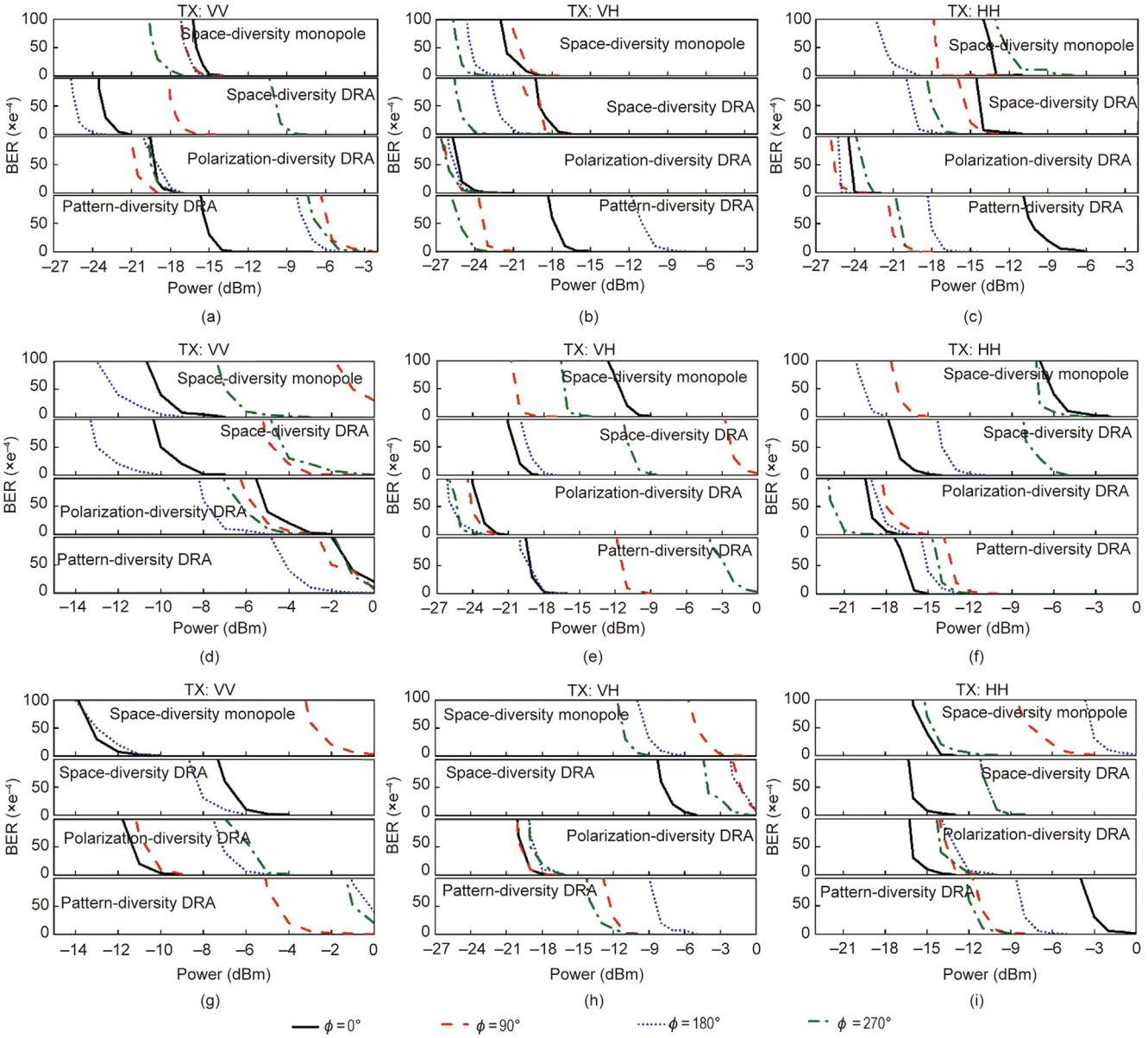

Fig. 21. Measured BERs for the four diversity antennas. (a–c) 2.44 GHz; (d–f) 5.20 GHz; (g–i) 5.80 GHz.

different directions. This implies that, when the transmitting power is fixed, the polarization-diversity DRA has the largest coverage distance with the most even signal around it.

With reference to the pattern-diversity DRA, the required power varies significantly in different directions. This is because one of the ports has broadside radiation patterns, resulting in non-uniform fields and different polarizations in the azimuthal plane. Similar phenomena can be observed at 5.2 and 5.8 GHz. Also, it is observed that, when the transmitting monopoles are HP, the VP space-diversity monopoles can still work. In actual application, monopole antennas do not have a pure polarization due to the inevitable curved feeding cable and the lack of radio frequency (RF) chokes. Owing to this feature, space-diversity monopole antennas can work regardless of the polarization of the incident electromagnetic wave. However, their performance is not stable in different directions.

According to the reciprocity principle, the same results will be obtained if the transmitting and receiving antennas are exchanged. It can be concluded that omnidirectional polarization-diversity antennas provide the most stable coverage among different diversity antennas. These antennas also have the largest coverage distance in most cases when different diversity antennas have comparable antenna gains.

6. Conclusions

Polarization-, pattern-, and space-diversity antennas were investigated for tri-band WiFi applications. These diversity antennas were also comprehensively compared for the first time in this paper. A novel tri-frequency polarization-diversity DRA fed by two loops and a probe was obtained for WiFi applications. By using a double-port feeding scheme and a stepped DRA structure, different-order TE modes could be excited and tuned to the 2.4, 5.2, and 5.8 GHz bands. Simultaneously, TM modes could also be tuned to the 2.4 and 5.2 GHz bands, while a probe mode was adjusted to 5.8 GHz. Polarization diversity was obtained with an isolation greater than 20 dB for the three bands. This polarization-diversity omnidirectional antenna was then fabricated and measured. The measured antenna gains (ϕ = 0°, θ = 60°) were 1.0, 0.3, and 1.3 dBi for the vertical polarization and 3.00, 2.00, and −0.75 dBi for the horizontal polarization in the three bands.

A novel tri-band pattern-diversity DRA fed by a probe and a slot was obtained. By using a stacked DRA structure, the bandwidth was efficiently enhanced for both the conical and the broadside radiation modes. Thus, the pattern-diversity antenna can cover the 2.4 GHz band and the entire 5 GHz WiFi band, with an isolation greater than 20 dB being obtained between its two ports. The measured antenna gains were 0.06, 0.96, and 0 dBi at (ϕ = 0°, θ = 60°) for the omnidirectional port in the three WiFi bands, and 6.8, 11.8, and 4.0 dBi at (θ = 0°) for the directional port.

To facilitate the comparison, a space-diversity omnidirectional DRA was also designed in the three WiFi bands. The measured gains at (ϕ = 0°, θ = 60°) were 2.7, 1.3, and 1.3 dBi in the three bands. The measured isolations between the two ports were 14, 22, and 26 dB in the three bands. To provide a reference, a commercial space-diversity monopole pair was also measured, with antenna gains of 0, 0.35, and 0.50 dBi within the three bands.

Furthermore, the BERs of the four diversity antennas were measured and compared. Three cases of antenna placement in end users were considered. It was observed that the polarization-diversity antenna had the most stable BER performance in different directions of the azimuthal plane. This implied that the signal coverage around the antenna was the most uniform. In most cases, the polarization-diversity antenna can provide the largest coverage distance. Also, it should be mentioned that DRAs were only used for the ease of their tri-band diversity designs, and the conclusions remain valid for other antenna types.

Acknowledgments

This work is supported in part by the Innovation and Technology Support Programme (ITSP) of the Innovation and Technology Commission (ITS/210/19), in part by the Young Scientists Fund of the National Natural Science Foundation of China (62001409), in part by Shenzhen–Hong Kong–Macao Science and Technology Project (Category C) (SGDX20210823104002018), and in part by 2022 Guangdong–Hong Kong–Macao Joint Innovation Funding Scheme (2022A0505030021).

The authors would like to thank Kam Man Shum and Man Shing Leung in state key laboratory of terahertz and millimeter waves of CityU for assisting in the experiment and taking the photographs, respectively. The technique support of engineers from Keysight is gratefully appreciated.

Compliance with ethics guidelines

Peng Fei Hu, Kwok Wa Leung, Kwai Man Luk, Yong Mei Pan, and Shao Yong Zheng declare that they have no conflict of interest or financial conflicts to disclose.

References

[1] Li Q, Yu X, Xie M, Li N, Dang X. Performance analysis of uplink massive spatial modulation MIMO systems in transmit-correlated Rayleigh channels. China Commun 2021;18(2):27–39.
[2] Hashemi H. The indoor radio propagation channel. Proc IEEE 1993;81(7):943–68.
[3] Cox D, Murray R, Arnold H, Norris A, Wazowicz M. Cross-polarization coupling measured for 800 MHz radio transmission in and around houses and large buildings. IEEE Trans Antennas Propag 1986;34(1):83–7.
[4] Chizhik D, Ling J, Valenzuela RA. The effect of electric field polarization on indoor propagation. In: Proceedings of IEEE 1998 International Conference on Universal Personal Communications; 1998 Oct 5–9; Florence, Italy; 1998.
[5] Turkmani AMD, Arowojolu AA, Jefford PA, Kellett CJ. An experimental evaluation of the performance of two-branch space and polarization diversity schemes at 1800 MHz. IEEE Trans Veh Technol 1995;44(2):318–26.
[6] Morshedi A, Torlak M. Measured comparison of dual-branch signaling over space and polarization diversity. IEEE Trans Antennas Propag 2011;59(5):1678–87.
[7] Fan Y, Liu X, Liu B, Li R. A broadband dual-polarized omnidirectional antenna based on orthogonal dipoles. IEEE Antennas Wirel Propag Lett 2016;15:1257–60.
[8] Guinvarc'h R, Serhir M, Boust F. A compact dual-polarized 3:1 bandwidth omnidirectional array of spiral antennas. IEEE Antennas Wirel Propag Lett 2016;15:1909–12.
[9] Ye LH, Cao YF, Zhang XY, Gao Y, Xue Q. Wideband dual-polarized omnidirectional antenna array for base-station applications. IEEE Trans Antennas Propag 2019;67(10):6419–29.
[10] Wu J, Yang S, Chen Y, Qu S, Nie Z. A low profile dual-polarized wideband omnidirectional antenna based on AMC reflector. IEEE Trans Antennas Propag 2017;65(1):368–74.
[11] Wen S, Xu Y, Dong Y. A low-profile dual-polarized omnidirectional antenna for LTE base station applications. IEEE Trans Antennas Propag 2021;69(9):5974–9.
[12] Huang H, Liu Y, Gong S. Broadband dual-polarized omnidirectional antenna for 2G/3G/LTE/WiFi applications. IEEE Antennas Wirel Propag Lett 2016;15:576–9.
[13] Quan X, Li R. A broadband dual-polarized omnidirectional antenna for base stations. IEEE Trans Antennas Propag 2013;61(2):943–7.
[14] Ando A, Kondo A, Kubota S. A study of radio zone length of dual-polarized omnidirectional antennas mounted on rooftop for personal handy-phone system. IEEE Trans Veh Technol 2008;57(1):2–10.
[15] Ta SX, Nguyen DM, Nguyen KK, Dao CN, Nguyen-Trong N. Dual-polarized omnidirectional antenna with simple feed and ultrawide bandwidth. IEEE Antennas Wirel Propag Lett 2020;19(5):871–5.
[16] Li W, Leung KW, Yang N. Omnidirectional dielectric resonator antenna with a planar feed for circular polarization diversity design. IEEE Trans Antennas Propag 2018;66(3):1189–97.
[17] Zou L, Abbott D, Fumeaux C. Omnidirectional cylindrical dielectric resonator antenna with dual polarization. IEEE Antennas Wirel Propa Lett 2012;11:515–8.

[18] Li Y, Zhang Z, Feng Z, Iskander MF. Design of omnidirectional dual-polarized antenna in slender and low-profile column. IEEE Trans Antennas Propag 2014;62(4):2323–6.
[19] Yang N, Leung KW, Wu N. Pattern-diversity cylindrical dielectric resonator antenna using fundamental modes of different mode families. IEEE Trans Antennas Propag 2019;67(11):6778–88.
[20] Li WW, Leung KW. Omnidirectional circularly polarized dielectric resonator antenna with top-loaded Alford loop for pattern diversity design. IEEE Trans Antennas Propag 2013;61(8):4246–56.
[21] Gray D, Watanabe T. Three orthogonal polarisation DRA-monopole ensemble. Electron Lett 2003;39(10):766–7.
[22] Liu X, Wu Y, Zhuang Z, Wang W, Liu Y. A dual-band patch antenna for pattern diversity application. IEEE Access 2018;6:51986–93.
[23] Dong Y, Choi J, Itoh T. Vivaldi antenna with pattern diversity for 0.7 to 2.7 GHz cellular band applications. IEEE Antennas Wirel Propag Lett 2018;17(2): 247–50.
[24] Chi PL, Itoh T. Miniaturized dual-band directional couplers using composite right/left-handed transmission structures and their applications in beam pattern diversity systems. IEEE Trans Microw Theory Tech 2009;57(5): 1207–15.
[25] Yan S, Vandenbosch GAE. Low-profile dual-band pattern diversity patch antenna based on composite right/left-handed transmission line. IEEE Trans Antennas Propag 2017;65(6):2808–15.
[26] Sun L, Zhang G, Sun B, Tang W, Yuan J. A single patch antenna with broadside and conical radiation patterns for 3G/4G pattern diversity. IEEE Antennas Wirel Propag Lett 2016;15:433–6.
[27] Fang XS, Leung KW, Luk KM. Theory and experiment of three-port polarization-diversity cylindrical dielectric resonator antenna. IEEE Trans Antennas Propag 2014;62(10):4945–51.
[28] Wang W, Zhao Z, Sun Q, Liao X, Fang Z, See KY, et al. Compact quad-element vertically-polarized high-isolation wideband MIMO antenna for vehicular base station. IEEE Trans Veh Technol 2020;69(9):10000–8.
[29] Amjadi SM, Sarabandi K. Mutual coupling mitigation in broadband multiple-antenna communication systems using feedforward technique. IEEE Trans Antennas Propag 2016;64(5):1642–52.
[30] Long S, McAllister M, Shen L. The resonant cylindrical dielectric cavity antenna. IEEE Trans Antennas Propag 1983;31(3):406–12.
[31] Mongia RK, Ittipiboon A. Theoretical and experimental investigations on rectangular dielectric resonator antennas. IEEE Trans Antennas Propag 1997;45(9):1348–56.
[32] Sabouni A, Kishk AA. Dual-polarized, broadside, thin dielectric resonator antenna for microwave imaging. IEEE Antennas Wirel Propag Lett 2013;12:380–3.
[33] LeungKW LEH, Fang XS. Dielectric resonator antennas: from the basic to the aesthetic. Proc IEEE 2012;100(7):2181–93.
[34] Karaboikis MP, Papamichael VC, Tsachtsiris GF, Soras CF, Makios VT. Integrating compact printed antennas onto small diversity/MIMO terminals. IEEE Trans Antennas Propag 2008;56(7):2067–78.
[35] Hu PF, Pan YM, Zhang XY, Zheng SY. Broadband filtering dielectric resonator antenna with wide stopband. IEEE Trans Antennas Propag 2017;65 (4):2079–84.